HEFAT2014
10th International Conference on Heat Transfer, Fluid Mechanics and Thermodynamics
14 – 16 July 2014
Orlando, Florida

JET IN CROSSFLOW: EXPERIMENTS ON THE INTERACTION OF FLOW-STRUCTURE AND COOLING EFFICIENCY

Lange, H.C. de*
*Author for correspondence
Department of Mechanical Engineering,
Eindhoven University of Technology,
Eindhoven,
The Netherlands,
E-mail: h.c.d.lange@tue.nl

ABSTRACT

The effect of imperfections in film-cooling nozzles on the flow fields and cooling effectiveness is studied. Measurements are performed using laser induced fluoresce, particle image velocimetry and thermo-chromic liquid crystal sheets. Different positions, shapes (square, triangular and round) and sizes (5-25% blockage) of imperfections are used to investigate the role of the nozzle geometry at different velocity ratios (0.15-1.50) with a fixed nozzle angle (37^o). Results will show that the position and size of the geometry disturbance are determining factors in the resulting cooling effectiveness, through their effect on the vortex-structures at the nozzle outlet. In some cases, the imperfect holes lead to a significantly improved performance, while in some other cases they deteriorate it.

INTRODUCTION

Film-cooling is one of the major techniques used in the protection of materials in gasturbines. Better cooling allows higher gas temperatures which leads to a better engine performance. The drilling of the nozzles can generate imperfections of the geometry, which (due the small size of the nozzles) can lead to imperfection size up to 25% of the nozzle diameter [1]. In this research we study how a discrete nozzle imperfection influences film cooling, when the film cooling process is simplified to a single jet in a cross flow over a flat plate.

The flow field for film cooling is characterized by `weak' jets, which are ejected into the cross-flow boundary layer through inclined holes. One of the first detailed papers which report the transverse jet in the cross flow was written by Bergeles et al. [2]. Morton and Ibbetson [3] analyzed the warp mechanism of the vortical structures. Fric and Roshko [4] studied vortical structures in the wake of the transverse jet experimentally. Kelso et al. [5] investigated experimentally the vortical structures in the jet cross flow interaction. The genesis and development of a counter rotating vortex pair was very well explained by Lim et al. [6].

In this paper, we will study the influence of an imperfection (of varying shape, size and position), which is fixed inside the hole, on these vortical structures. And, in its turn, the influence of the change in flow structure on the adiabatic film cooling effectiveness. As a reference, experiments are conducted with a "perfect" (without any artificial imperfection) hole.

First, experiments are shown using Laser induced fluorescence (LIF) for visualizations and Particle Image Velocimetry (PIV) for studying the flow field. These tools are used to study the effect of round imperfections at different positions in the nozzle. The vortex structures recognized in the jet in crossflow interaction are depicted in figure 1. Four major coherent structures are found: a counter-rotating vortex pair (in the core of the jet), windward, leeward and spiral (at the nozzle sides) vortices.

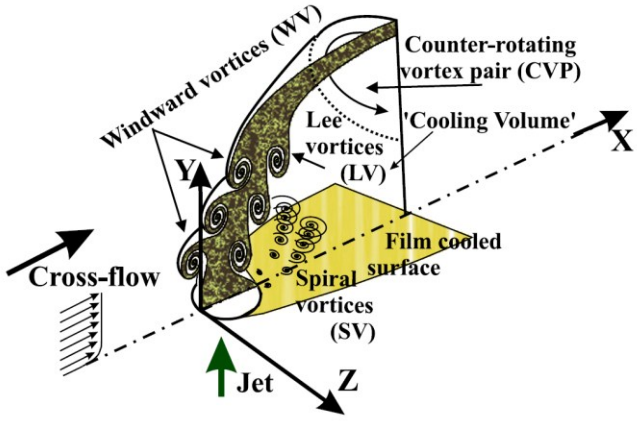

Figure 1 Vortical structures resulting from jet-crossflow interaction.

Next, the film cooling effectiveness is measured by means of liquid crystals thermography (LCT). Using integral cooling values, the effect of imperfections of different shapes and sizes can be identified. Furthermore, the changes in cooling effectiveness will be connected to the known changes in the flow-field.

NOMENCLATURE

D	[m]	Nozzle diameter
L	[m]	Nozzle Length
X	[-]	x/D (x: streamwise distance from nozzle leading edge)
Z	[-]	z/D (z: spanwise distance from nozzle centreline)
Twall	[K]	Wall temperature
T0	[K]	Main stream inlet temperature
Tjet	[K]	Jet inlet temperature
Q	[m^3/s]	Jet volume flow
V0	[m/s]	Main stream velocity
V	[m/s]	The local velocity
Vmean	[m/s]	The image mean velocity
Vjet	[m/s]	Mean Jet Velocity
VR	[-]	Velocity ratio
v'	[m/s]	The disturbance velocity
η	[-]	Adiabatic cooling effectiveness
Φ	[-]	Equivalent cooled surface
Ω	[1/s]	Vorticity

EXPERIMENTAL SETUP

Water channel

The experiments were performed in a closed-return water channel at the Technische Universiteit Eindhoven (Eindhoven University of Technology) shown in figure 2.

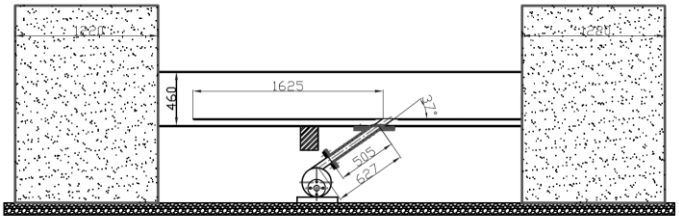

Figure 2: schematic of water channel

The water channel consists of two reservoirs and a closed test section. Incoming and outgoing reservoirs are connected with three pipes each with their own pump. The test section has a length of 3170mm, a width of 600mm and a height 450mm. The top- and side-walls of the closed test section made of glass to allow optical measurements.

To obtain a water flow with a uniform velocity, a pair of flow straighteners was placed at the beginning of the test section. The flow straightener consists of rectangular combs (with a characteristic rectangle 6.1x5.2mm and a metal mesh (with a characteristic dimension 1.5mm. This combination provides uniform flow with a turbulent intensity lower than 1% in the test section. To investigate the influence of turbulence (in the last section of this paper), a static grid can be added to increase the main stream turbulence to about 7%. Streaming energy is supplied with three pumps fed from the incoming reservoir. The speed inside the test section can be varied from 0 till 0.35m/s.

The flat plate is mounted at 0.3m from the inlet section at 5cm above the channel floor. Its leading edge is sharp and suction below the plate is used to prevent flow separation. Leading edge visualizations and PIV measurements have been used to set the suction pump to ensure a smooth leading edge flow.

Nozzle geometry

The jet is ejected through an inclined smooth pipe into the cross-flow boundary layer. It enters though the bottom of the channel and is connected to the flat plate. The leading edge of the jet injection nozzle is located 1625mm from the plate leading. The diameter of the pipe is D = 57mm and the inclination angle is 37° (figure 3). The length of the pipe L is equal to 10D.

The jet injection system is independent of the water channel. It consists of a tank, pump, plenum and the pipe. To eliminate the influence of the pump, the plenum is fed symmetrically from the sides. Furthermore, a flow-straightener supported with a fine mesh is built-in at the inlet of the pipe to ensure homogeneous flow.

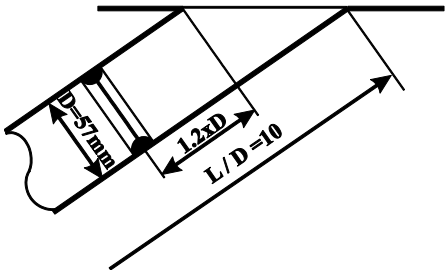

Figure 3: schematic jet inlet (with imperfection)

The influence of different imperfections on the jet cross-flow interaction has been investigated for varying mass blowing ratios. Since the density is constant and the same fluid was used for the jet and cross-flow the mass blowing ratio equals the velocity ratio (*VR*):

$$VR = \frac{Vjet}{V0} \tag{1}$$

Where *V0* is the main stream velocity. The averaged jet velocity (*Vjet*) was calculated as the ratio of the jet volume flow and the pipe cross-section:

$$Vjet = \frac{4Q}{\pi D^2} \tag{2}$$

With *Q* the jet volume flow.

The experiments have been conducted with a smooth nozzle and with nozzles containing a discrete imperfection. The discrete imperfection, generated during the production process

of a film cooling hole, is simulated with a number of different shapes and sizes of imperfections (shown in figure 4). Most experiments shown concentrate on the imperfection cases: inner-torus 1 and inner-torus 2. These imperfections are the circular shaped figure 4 right column case 3) disturbances placed at the outlet of the nozzle (inner-torus 1) or at 1.2D in the nozzle (inner-torus 2, as shown in figure 3). The case inner torus 3 (which will be treated in the section on effectiveness) is the same disturbance placed 2.5D inside the nozzle.

When the issue of the effect of shape and size on the effectiveness are studied, the different geometries in figure 4 are placed at position 2 (at 1.2D inside the nozzle).

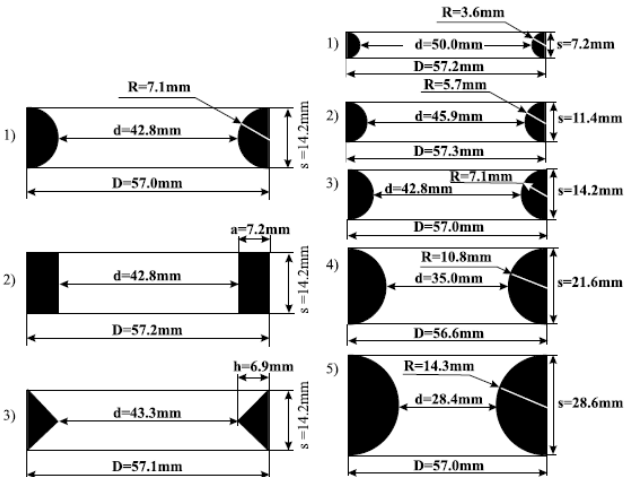

Figure 4: different shapes and sizes of imperfections

EXPERIMENTAL METHODS

Laser induced fluorescence (LIF)

Laser induced fluorescence (LIF) is applied to visualize the flow field. The intensity of this fluorescence is, in general, a function of the species concentration and fluid temperature. Fluorescein sodium salt ($C_{20}H_{10}Na_2O_5$), which has been used in our experiments, is only concentration sensitive. The fluorescein is added to the flow in the jet, thus lightning up the cooling fluid.

Particle image velocimetry (PIV)

Flow field measurements are performed by means of Particle Image Velocimetry (PIV). As tracer particles, 20μm polyamid seeding particles are used added to both the jet and main stream fluid.

A dual-pulse Nd:Yag laser (λ = 532nm) is used to illuminate the tracers. To form a 2mm thick laser sheet, a negative lens and rectangular diaphragm were used. The images are recorded with CCD cameras (Kodak Megaplus 1008x1018 pixels, 10bits) and stored on hard disks using the acquisition software VideoSavant. The sampling frequency is 15Hz, which is limited by the Nd:Yag laser. The PIV software, used to process the data, has been developed at the Technische Universiteit Eindhoven. It uses a standard algorithm to cross-correlate particle images in interrogation areas with sub-pixel interpolation.

The PIV measurements are conducted in several plane orientations. In the wall-normal plane along the central line of the flat plate, two CCD cameras are used. The first camera position captures the flow field in front of the nozzle till the nozzle center. The measurement field of each camera was 80x80mm. Larger view measurements were also conducted with a window size of 200x200mm. The flowfield in the wall parallel planes are captured similarly (now with the cameras above the channel).

In order to capture the counter-rotating vortex pair in the wall-normal spanwise plane, a mirror technique is used. The mirror is placed inside the water channel at X=12. The measurements are performed at 8 streamwise positions (between X = 0.8 and 5.7). The size of the images varied from 120x120mm (at X=0.8) until 90x90mm (at X=5.7). The perspective error was corrected by capturing only the flow of the main stream at each measured position for all velocity ratios.

Vortices in a flow field are determined from the disturbance velocity (v'):

$$v' = v - vmean \qquad (3)$$

With v the local velocity and *vmean* the image mean velocity. To determine the mean velocity, the average flow field is determined by averaging and processing 250 frame pairs per measurement.

Liquid cristal thermography (LCT)

Liquid crystal thermography has been used to measure temperature on the plate wall. To undertake these measurements two coated polyester sheets of thermochromic liquid crystals (TLCs) are fixed on the plate wall. The TLC sheets have been produced by Hallcrest (R20C5W). The red colour should start at 20 degrees and the bandwidth is 5^{o}C. The measurements are conducted using wide band technique. The temperature in the channel has been measured by means of a mercury thermometer with an accuracy of 0.05^{o}C. The temperature in the channel is measured just before the beginning of an experiment. The jet temperature is adjusted and measured with the same thermometer to eliminate the bias. Images of the TLC sheets were taken with an analog three CCD video camera (JVC KY-F30). The camera is placed above the channel to look perpendicularly at the sheets. A light source is located at the side of the channel. A sample result is shown on figure 5 (top).

Calibration has been conducted in situ by heating water in the channel. The calibration accuracy is within 0.1^{o}C in the red-green zone and within 0.3^{o}C degree in the blue zone. Using this calibration the raw LCT image is turned into a wall temperature distribution (figure 5 (middle)).

The Plexiglas surface is treated as an adiabatic wall. Therefore, the adiabatic cooling effectiveness (figure 5 (bottom)) is calculated from the temperature measurements:

$$\eta = \frac{Twall - T0}{Tjet - T0} \tag{4}$$

Here *T0* is the temperature of the cross flow, *Tjet* is the jet temperature and the temperature measured on the plate wall is denoted as *Twall*.

To investigate the effect of the velocity ratio simultaneously with the effect of the imperfection position, its shape and size the equivalent cooled surface Φ is defined as:

$$\Phi = \int_{0}^{\infty}\int_{-\infty}^{\infty} \eta dZdX \tag{5}$$

The integration in *x*-direction is of course limited by the length of the measurement field. The same goes for the *z*-direction, but there η=0 at the edge of the field.

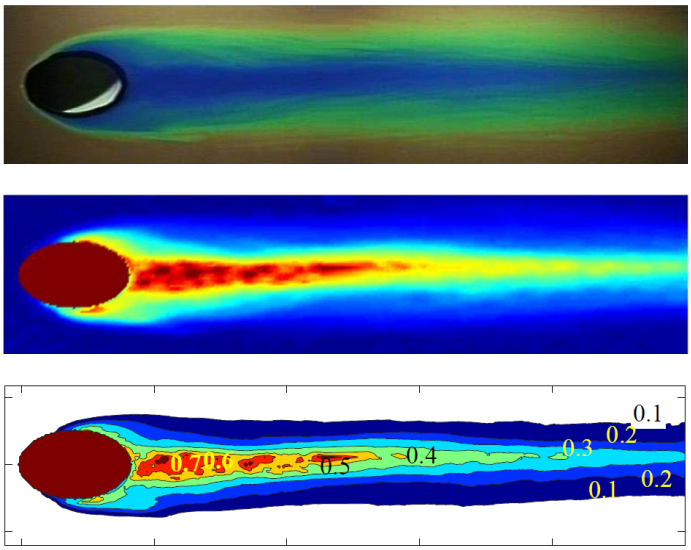

Figure 5: The raw LCT image (top) turned into a temperature field (middle) and the resulting adiabatic cooling effectiveness (bottom)

FLOW FIELDS

Flow characteristics

The cross-flow with the free stream velocity (*V0)* of approximately 0.2m/s is superimposed on the submerged jet. Therefore, the jet is deflected and pushed towards the plate surface. The radius of the bend depends on the velocity ratio. For *VR*<2, the jet cross-flow interaction forms two main zones: an undisturbed zone of the free stream and a cooling volume. These two zones are separated by a shear layer.

To pinpoint the border between the zones LIF visualisations were conducted. The jet was painted with a fluorescent dye and injected into the cross flow boundary layer.

Some typical instantaneous results of LIF visualisations are presented in figure 6 (for a perfect nozzle at four velocity ratios *VR*= 0.25, 0.50, 1.00 and 1.50). At the low velocity ratios, such as *VR*=0.25 or 0.50, the fluid that leaves the nozzle is spilled over the plate surface. The jet `body' is not detected and the plate wall is very well covered along the centerline. For increasing velocity ratios, the jet `body' becomes more and more recognizable inside the cooling volume.

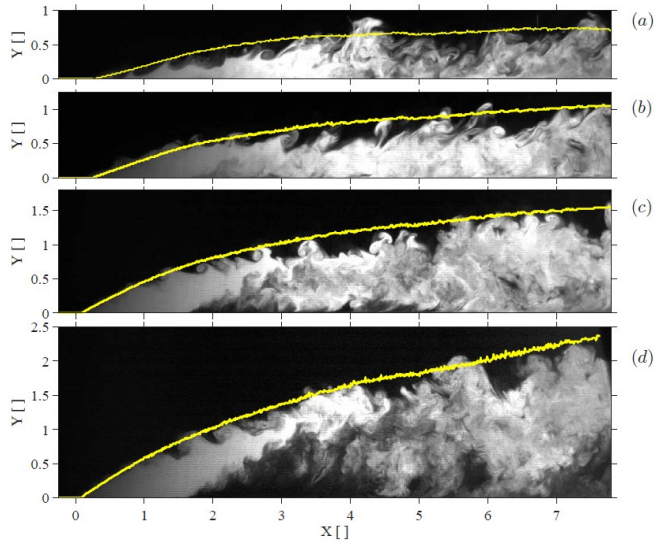

Figure 6: The snapshots of LIF visualisations along the central plane *Z* = 0 for a perfect nozzle at four velocity ratios: a) 0.25, b) 0.50, c) 1.00 and d) 1.50. The yellow lines indicate the borders between the cooled volume and free stream obtained from average images.

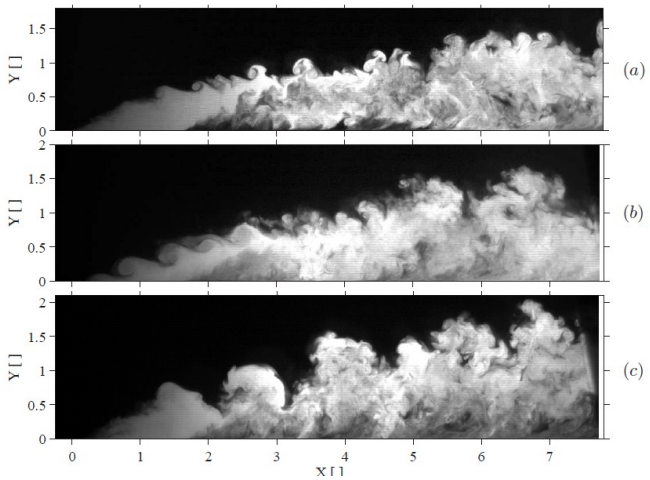

Figure 7: Snapshots of LIF visualisations along the central plane *Z* = 0 at *VR*=1.00 in: a) the perfect b) inner-torus 1 and c) inner-torus 2 cases.

As an indication of the influence of the imperfections, figure 7 shows the results for *VR*=1 for different nozzle geometries. The perfect nozzle is compared with the torus imperfection place at the nozzle outlet (inner torus-1) and with the torus placed approximately 1*D* inside the nozzle (inner torus-2, as shown in figure 3). Small positive vortices are formed in the perfect case. Inner-torus 1 produces stronger vortices, which rotate in the same direction as the windward vortices in the perfect case. At the lee side, the negative vortices can only faintly be seen. These vortices interact around *X*=3.0. While inner-torus 1 reduces mixing with the cross-flow

fluid, inner-torus 2 increases it, except in the vicinity of the nozzle trailing edge. Remarkable structures are generated by inner-torus 2. The jet leaves the nozzle and around X=2.2, a large penetrating injection of main stream fluid is detected. Downstream of this penetration a cloud, which mostly contains the jet fluid, moves away from the plate surface. Apparently, the inner-torus 2 case leads to intermittent gulps of jet fluid entering into the boundary layer.

Lee- and windward vortices

To analyze the shedding process, combined zoomed PIV and LIF measurements are performed. In figure 8, the average and an instantaneous flow fields are presented for a perfect nozzle at *VR*=0.90. In the average flow field (figure 8a), the lee shear layer is visible. Below this shear layer, back flow is detected at X=2.2. Further downstream, accelerated flow is detected near the plate wall. This higher velocity indicates a central plane penetration. The instantaneous flow field (figure 8b) gives a totally different perspective. The LIF snapshot depicts typical shedding structures along the windward (upper) shear layer and lee (inner) shear layer. The PIV flow field shows a flow (jet `body') in-between the windward and lee vortical structures, which is coherent and stable. The flow below the lee shear layer (between the jet and the plate surface) appears to be fully turbulent.

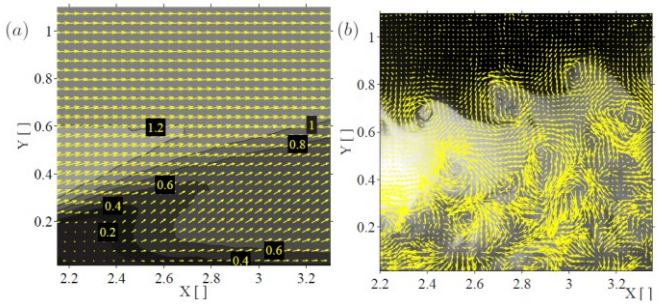

Figure 8: The flow for the perfect nozzle at $V\,R$ = 0:90 a) The average velocity field (over 500 image pairs) and b) an instantaneous LIF snapshot with the disturbance velocity vectors from PIV.

The vorticity (Ω'_z) of lee and windward vortices produced in the perfect case are shown in figure 9, where

$$\Omega'_z = \frac{D}{V0}\left(\frac{\partial v'_y}{\partial x} - \frac{\partial v'_y}{\partial y}\right) \qquad (6)$$

In this experiment, the instantaneous results of a combined LIF and PIV measurement at three subsequent camera positions are used.

Small vortical structures shed the windward shear layer. They are amplified by the shear-layer (Kelvin-Helmholtz) instability. At the nozzle leading edge, the local velocity of the jet is slightly larger than the cross flow. Therefore, small positive vortices are generated with $\Omega'_z \sim 5$ inside the vortex. The surface of the windward vortex does not exceed 2% of D^2.

At the same time negative lee-ward vortices are produced at the nozzle trailing edge. The flow separates over the nozzle trailing edge, roles up and forms a lee vortex. The shedding frequency is very high and could not be detected with applied PIV system. The lee vortices have negative vorticity, which is again due to the jet velocity being locally higher then the velocity in the boundary layer (and, again, this process is amplified by the Kelvin-Helmholts instability, which now tends to `roll' negative vortices). The lee vortices merge with the positive vortices at X~ 3.3.

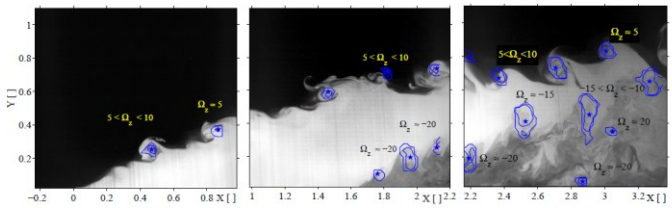

Figure 9: The vortical structures superimposed on the instantaneous LIF image for a perfect nozzle at $V\,R$ = 0.90

Similarly, for the inner torus-2 case the LIF and PIV images are compared in figure 10. This time, a large positive vortex is detected at the windward side of the hole. This vortex is 4.8 times larger than the windward vortex detected in the perfect case. It emerges from the nozzle, which could mean that it is a part of a ring vortex generated at the imperfection (inside the nozzle). When this windward vortex leaves the nozzle, the cross-flow penetrates the windward side of the jet and rolls into a quasi-horseshoe vortex. This vortex is much smaller than the positive counter rotating part.

At the lee side, the `separation' vortex warps with the size comparable to the windward vortex. While the windward vortex sheds the upstream (windward) shear layer, the lee vortex flows along the inner (lee) shear layer. At X~ 1.5, they start to interact and produce a burst. The subsequent mixing leads to a reduced fluorescence concentration (visible from X~2.2). The vortex ring appears as a cloud of jet fluid, detaching from the cooling volume and penetrating into the free stream.

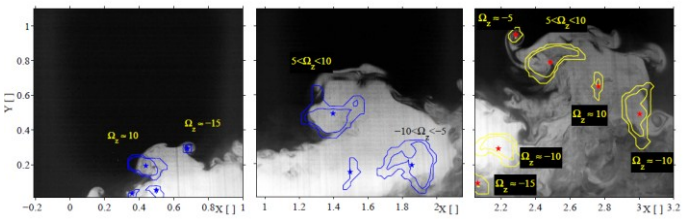

Figure 10: The vortical structures superimposed on the instantaneous LIF image for inner torus-2 at V R = 0.90

Spiral vortices

Next, we examine the flow in the wall-parallel plane. The average flow field in the plane Y=0.15 (a horizontal plane covering the nozzle) for a perfect nozzle at varying velocity ratios is shown in figure 11 (bottom), while figure 11 (top) shows an instantaneous combined PIV/LIF result.

The results show two vortical structures (spiral vortices) in the vicinity of the nozzle trailing edge. At *VR*=0.45, these

structures are still hardly recognizable. The average vorticity has a maximum of 2 in the centers of the vortices.

At increased velocity ratios, the vortices become stronger and larger. At *VR*=0.90, the vorticity reaches 5 and the vortical structures cover the trailing edge of the hole. At *VR*=1.25, the vortices are a bit stronger and larger than at *VR*=0.90. The effect of these vortical structures can be seen in the upper row of figure 11, there is no fluorescence in the kernel of the spiral vortices. This means that the fluid from the nozzle does not penetrate these structures. Therefore, at larger velocity ratios, the jet lifts and allows cross-flow (main stream) penetration. This could certainly decrease the film cooling effectiveness.

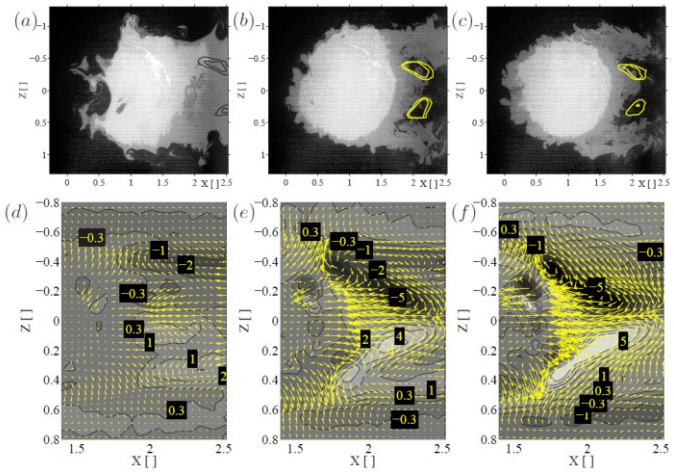

Figure 11: Horizontal measurements with a perfect nozzle. Visualizations (top) and (at bottom) the average flow field with its vorticity (Ω_y) in the background for (from left to right) *VR*= 0.45, 0.90 and 1.25.

Figure 12 shows the same experimental results but now for the inner torus-2 case. It is obvious that in all cases (at all velocity ratios) the inner-torus 2 case is different from the percat nozzle.

At low velocity ratio (*VR*=0.45), the jet is blocked at the wind ward side and the cross-flow can also penetrate the jet at the side rims. Overall, the mean vorticity appears to be much lower than in the perfect case. However, the impingement of main stream fluid into the jet structure gives a much less structured jet.

For larger velocity ratios, the side penetration is smaller but still occurs. A most intriguing process is detected downstream of the nozzle. As seen earlier (f.e. in figure 7c), the flow with inner-torus 2 is more chaotic than in the perfect case, but, here it shows a better coverage of the plate wall. The helical vortices are still present and the penetration from the side is still detected. However, the very unstable flow generated by inner-torus 2 ensures a better coverage and, therefore, a higher film cooling effectiveness can be expected in the vicinity of the hole.

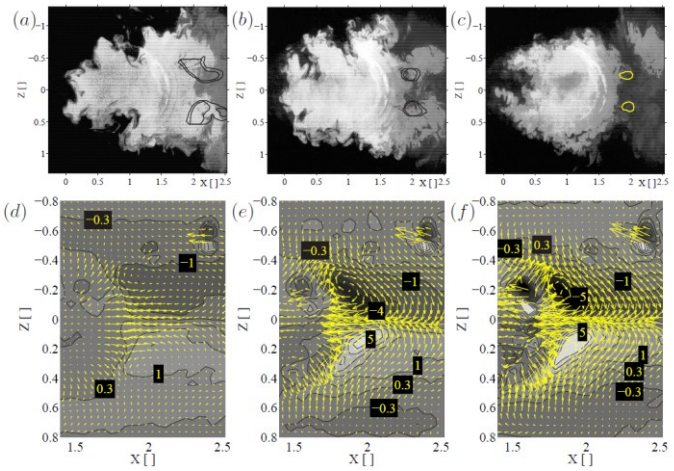

Figure 12: Horizontal measurements with inner-torus 2. Visualizations (top) and (at bottom) the average flow field with its vorticity (Ω'_y) in the background for (from left to right) *VR*= 0.45, 0.90 and 1.25.

Counter-rotating vortex pair (CVP)

The largest and probably most influential vortical structures generated by the jet cross-flow interaction are two vortices which are called the counter rotating vortex pair (CVP) or steady kidney vortices. These can be studied using the wall-normal spanwise plane measurements (the mirror setup).

In figure 13, the vectors of the average velocity and contour lines of turbulence intensity (Tu%) are depicted (from top to bottom) for the perfect, inner-torus 1 and inner-torus 2 cases at *VR*=1.00 in the plane X=2.2.

CVP in the inner-torus 1 case is closest to the plate wall and has the largest Tu% in the centers of vortices. A very large arch of strong Tu% is found in the case of inner-torus 1. This arch is absent in the perfect case and is turned into a large circle in the case of inner-torus 2, which values are smaller than of inner-torus 1. Tu% is similar in the centers of CVP for the perfect and inner-torus 2 cases and it is two times smaller than in the inner-torus 1 case. The large values of Tu% correspond to the intensive mixing detected by means of LIF (not shown).

Clearly, the shape and size of CVP change from case to case. They are small but relatively high in the perfect case. In the case of inner-torus 1, CVP has a shape of a mask at X=2.2; the vortices are closer to the plate wall and stretched along the Z axis. In the case of inner-torus 2, the vortices are very large with a kidney shape. On the other hand, the calculated vorticity (not shown) is comparable for all of them.

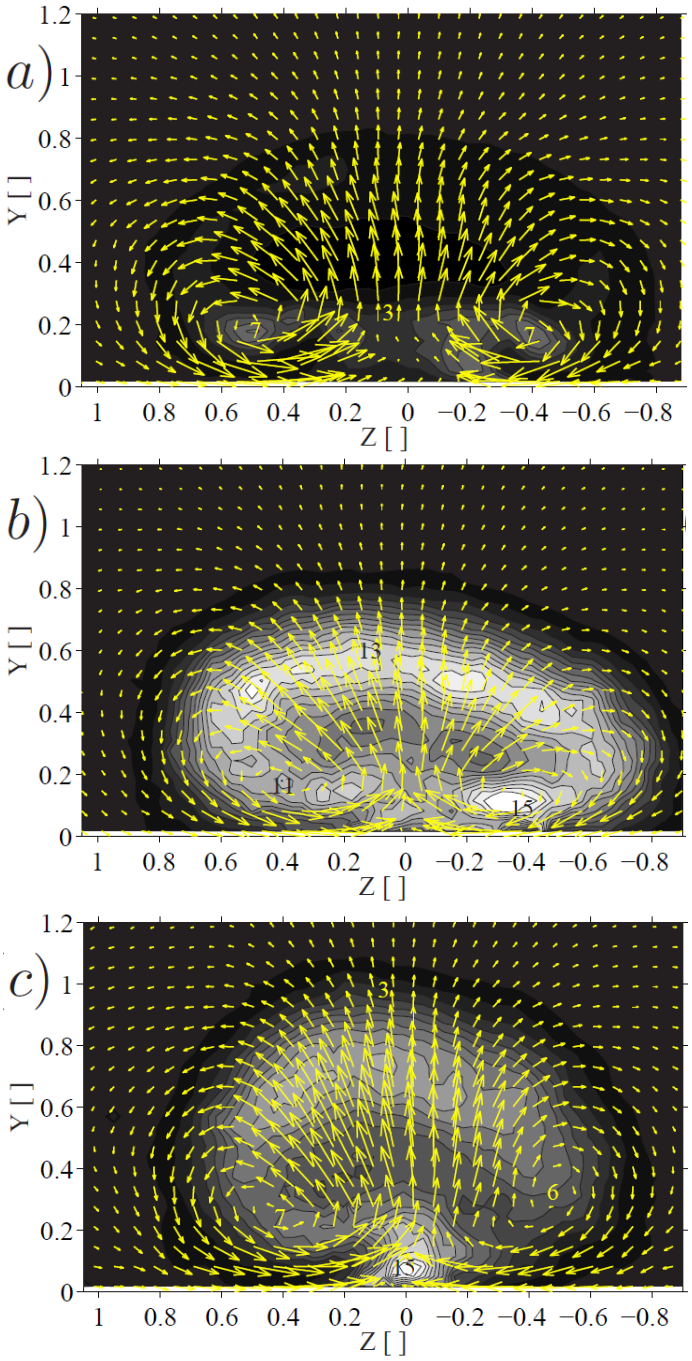

Figure 13: Lateral measurements at X=2.2 and *VR*=1.00 for(top to bottom) for a) perfect nozzle, b) inner-torus 1 and c) inner-torus 2. The arrows indicate PIV-measured velocity and gray-scale indicates the local turbulence intensity (Tu%)

Analysis

The shape and structure of the vortices generated under the influence of different imperfections can now be analyzed. In figure 14 a schematic overview of the changing in vortex generation is given.

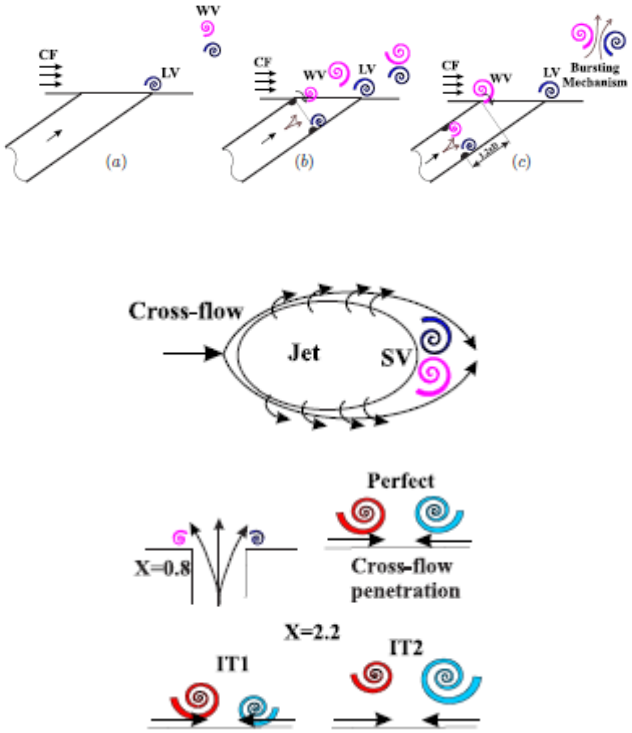

Figure 14: schematic of vortical structures generated at nozzle exit from top-to-bottom: lee- and windward vortices, spiral vortices and counter-rotating vortex pair.

The lee- and windward vortices generated in the perfect case along the central plane Z=0 are sketched in figure 14 (top) a. The windward vortices are small in the perfect case and they grow under the influence of the Kelvin-Helmholtz instability. In the vicinity of the nozzle, the vortices are positive at *VR*~1 and by decreasing the jet velocity they change the sign of rotation. At the lee side, the jet separates over the nozzle trailing edge and negative lee vortices roll up. Lee vortices shed a second (lee) shear layer and they can merge with the windward vortices or they can be advected alone, along the windward shear layer. These vortices do not have a strong influence on heat and mass transfer. They can form unsteady kidney or anti-kidney vortices in the windward shear layer.

At the imperfections (inner-torus 1 and 2) a ring vortex rolls up inside the nozzle at the imperfection. This vortex ring does not reach the nozzle rim at one time (the imperfection at the leading edge is much closer to the rim thn that of the trailing edge). Therefore, the paths at the wind- and leeward side are different. This means that the vortex ring breaks into the large and strong windward vortex, rim vortices and the lee vortex. The windward vortex is advected along the leading edge (windward) shear layer while the lee vortex shed the trailing edge (lee) shear layer.

Inner-torus 1 produces much larger positive vortices at the windward side (see figure 14 (top) b). The jet boundary

layer separates over the imperfection at the nozzle exit and rolls up into a windward vortex.

A similar scenario occurs if inner-torus 2 is inside the hole. They merge and form a burst (see figure 14 (top) c). This burst forms a cloud, which mainly contains the jet fluid. This cloud tends to leave the cooling volume and penetrate the free stream. These bursts are quasi-regular and they also induce jet oscillations.

In the horizontal plane two vortices (the spiral vortices) are detected in the average flow fields (see figure 14 (middle)). They warp at the lee side in the vicinity of the nozzle trailing edge. These vortices are detected in all cases and they have probably the same origin. The jet is bent by a cross-flow and accelerated at the lee side. Due to the curved path and the acceleration, the Coriolis force points toward the free stream. This force is balanced by the pressure difference, which implies lower pressure in the cooling volume than in the free stream. Therefore, the cross-flow penetrates the cooling volume near the nozzle trailing edge. Fluid lumps and vorticity blobs are pushed towards the jet lee side. They have a small momentum and they cannot penetrate the jet, instead they are lifted and twisted. They move along a spiral and form the spiral vortices. In the instantaneous measurements, these vortices are not detected in a horizontal plane. But the flow visualisation and average flow fields confirm this motion.

In the perfect case, the jet is coherent and the spiral vortices mix mostly the cross-flow fluid. This may rapidly decrease the film cooling effectiveness in the nozzle vicinity. After the jet `attachment', the effectiveness is expected to increase in the perfect case. The inner-torus disturbs the jet, breaks its coherence and more effectively covers the near nozzle region. For inner-torus 1 and 2, the spiral vortices mix jet fluid with the cross-flow. This may lead to a higher effectiveness in the nozzle vicinity compared to the perfect case.

The largest and probably the most important structure in the jet cross-flow interaction is CVP (figure 14 (bottom)). These vortices, which are generated at the nozzle rims, are strong and small. They are advected and stretched by the cross-flow. The vortex pair will induce a positive wall-normal movement according to the Biot-Savart law. Therefore, CVP lifts. As the CVP is very strong and can feed on vorticity in the cooling volume. it can sustain very long in the flow field.

In the perfect case, the CVP lifts and improves the cross-flow penetration. `Perfect' CVP-s are stable, symmetrical and relatively coherent. It acts as a propeller and improves the cross-flow penetration. Further downstream, the CVP grows and reaches the plate wall. The viscous stresses at the wall are strong and reduce the cross-flow penetration.

In the inner-torus 1 case, the CVP is stable as the average vortex but it is unstable in instantaneous flow fields. Windward and lee vortices induce jet oscillations, which affect the CVP. The instantaneous vortices are not symmetrical and, therefore, the lifting is different and smaller. CVP stays closer to the plate wall and the strong cross flow penetration is prevented. The generated CVP is also less coherent then in the perfect case and dissipates more. Although the mixing is strong, mostly jet fluid is transported by the CVP. Hence, a higher effectiveness may be expected than in the perfect case.

Inner-torus 2 produces a bursting mechanism. The large portion of the jet fluid tends to leave the cooling volume in the vicinity of the hole. Therefore, the CVP is not pushed towards the plate wall as in the case of inner-torus 1. On the contrary, CVP lifts and grows. The cross-flow penetrates towards the central plane and probably decreases the effectiveness. The instantaneous CVP is unstable as in the inner-torus 1 case. But the bursts enable the cross-flow penetration along vertical planes. This increases mixing with the main stream fluid and probably reduces the effectiveness.

ADIABATIC COOLING EFFECTIVENESS

Next, we can compare the adiabatic effectiveness (η) for different geometries and different velocity ratios. The results for a perfect nozzle and the inner torus-1 and -2 case are given in figure 15, 16 and 17 for *VR*=0.50, 1.00 and 1.50, respectively. The most striking feature is that the perfect case does not outperform the imperfect cases; the inner torus-1 case seems to give optimal adiabatic effectiveness for all velocity ratios. By comparison, the perfect nozzle appears to have its optimal cooling spot further away from the nozzle exit; the re-attachment point of the jet seems to lay further downstream. On the other hand the inner torus-2 case (with its highly turbulent mixing) has its optimum very close to the nozzle trailing edge and, through mixing has a quite uniform cooling decrease.

For *VR*=0.5 (figure 15), the influence of the imperfection is barely visible. In the perfect case, the cooled surface (η=0.1) is elongated. At the end of the measurement field, an effectiveness of 0.3 is detected. The maximum (η~0.6) is detected in the vicinity of the nozzle but not at its trailing edge. For inner-torus-1, the film cooling effectiveness is quantitatively similar to the perfect case but is better distributed with more spread in the lateral direction. Inner-torus 2 deteriorates the effectiveness and narrows the cooled surface. The maximum effectiveness (η~0.5) is detected closer to the trailing edge of the nozzle.

Increasing the velocity ratio to 1.00 (figure 16) decreases the overall film cooling effectiveness in all cases. For the perfect nozzle, the effectiveness is around 0.1 in the vicinity of the nozzle trailing edge. It reaches a maximum of 0.4 (at about 2D from the trailing edge) and then decreases continuously to 0.2 at the end of the measurement field. The lateral coverage of η=0.1 is less than 1D in the perfect case. Inner-torus 2 gives its maximum effectiveness (η~0.3) at the trailing edge of the nozzle and decreases continuously downstream. The most striking is the enhancement of effectiveness and the surface coverage by the presence of inner-torus 1. The maximum effectiveness is over 0.5 and the maximum width is approximately equal to 2D. η=0.3 is found at the end of the measurement field which is 50% higher than in the perfect case.

At *VR*=1.50 (figure 17), there is no cooling in the vicinity of the nozzle in the perfect case. The contour of η=0.1 appears at X~3.1 and extends till the end of the measurement field with the lateral coverage of 0.5D. Inner-torus 2 gives a bit wide but shorter cooled surface with rather similar values. It is, again,

remarkable that inner-torus 1 ensures the good film cover with the maximum effectiveness of 0.3 and the lateral coverage of 1.5D (with η ~0.2 at the end of the measurement field).

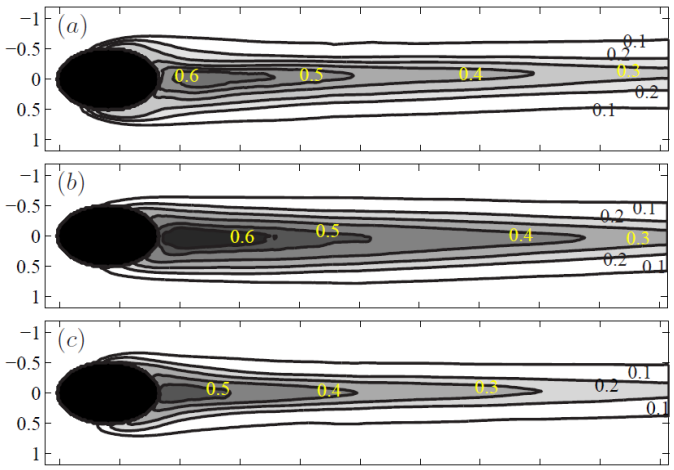

Figure 15: The film cooling effectiveness for *VR*=0.50 for a) the perfect nozzle, b) inner-torus 1, c) inner-torus 2

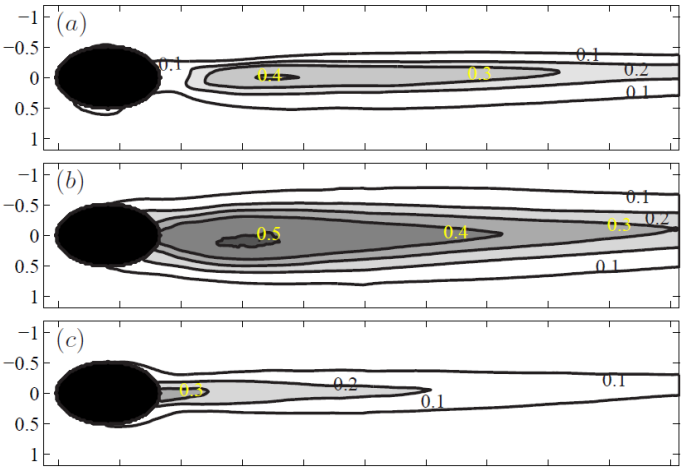

Figure 16: The film cooling effectiveness for *VR*=1.0 for a) the perfect nozzle, b) inner-torus 1, c) inner-torus 2

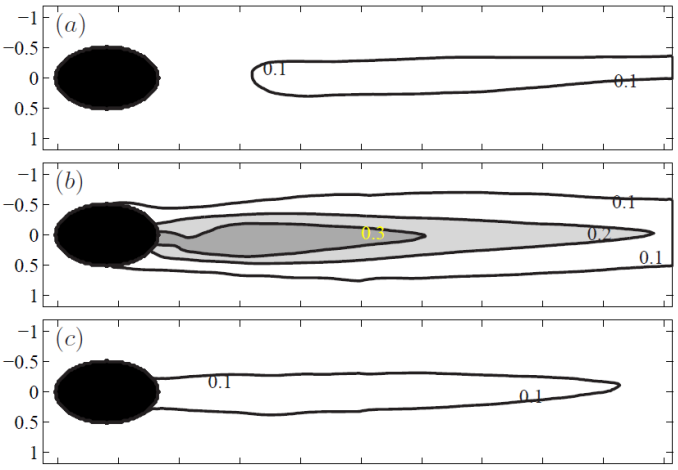

Figure 17: The film cooling effectiveness for *VR*=1.50 for a) the perfect nozzle, b) inner-torus 1, c) inner-torus 2

The most dominant vortical structure at higher velocity ratios (*VR*>1) is the counter rotating vortex pair (CVP). This CVP is strong and coherent. It lifts the jet and enables the cross-flow penetration. Therefore, the cooling effectiveness is low in the vicinity of the trailing edge for the perfect case at *VR*=1.00 and (almost) absent at *VR*=1.50. Inner-torus 2 generates bursts of large windward and leeward vortices. This induces jet/main flow mixing and, as a result, the effectiveness is decreases. The bursting mechanism is not detected in the case of inner-torus 1. In this case, the large windward vortices push the jet towards the plate wall and induce CVP instability. The cooling volume is comparable to the perfect case but the CVP stays closer to the wall and mostly mixes the jet fluid. Therefore, the effectiveness is much larger than in the perfect and inner-torus 2 cases.

Equivalent cooled surface

In figure 18a, the equivalent cooled surface for the perfect case and the inner-torus at different positions is shown. At *VR*=0.15, Φ ~ 3.2 in all cases. Φ increases and reaches its maximum of 3.6 at *VR*=0.25 in the perfect case. At this low velocity ratio, the imperfections have a very small influence on the equivalent cooled surface. The imperfection influence starts to be visible at *VR*=0.50. Inner-torus 1 improves Φ by 16% while inner-torus 2 deteriorates it by 27%. The influence of the triple imperfection (using inner-torus-1 2 and 3 simultaneously) is negative which indicates the dominance of inner-torus 2. Inner-torus 3 does not show any significant effect.

At the velocity ratio 0.70, Φ is 2.0 in the perfect case. Inner-torus 1 creates the largest Φ of 4.1. This is 100% more than in the perfect case. Inner-torus 2 reduces the effectiveness and therefore Φ by 29%. The equivalent cooled surface produced by means of the triple imperfection is somewhere between the one of the effectiveness produced by inner-torus 1 and inner-torus 2.

At *VR*=1, Φ drops to 1.7 in the perfect case but relative to the other cases, it does not change. At this *VR,* a small influence of inner-torus 3 is detected. Although this change is a bit larger than the measurement error, it can be concluded that the film cooling effectiveness is rather sensitive to small changes of *VR* around *VR*=1.00. The benefit of inner-torus 1 rises with the further increase in *VR* while the negative effect of inner-torus 2 decreases. At the largest measured *VR*=1.50, Φ equals 0.67in the perfect case. The negative influence of inner-torus 2 vanishes and it increases Φ by 23%. The positive contribution of inner-torus 1 is +1.69 or 253%.

Turbulence intensity

To obtain a higher turbulence intensity (Tu%), a static grid was placed at the entrance of the test section. This means that the main stream turbulence intensity rises to about 7%. The resulting equivalent cooled surface in this case is depicted in figure 18b. The position of the imperfections and *VR* are varied. The cooling for the perfect nozzle shows to be fairly independent of the turbulence intensity. Only at the velocity ratio of 0.57, Tu% reduces the film cooling effectiveness in the perfect case.

The turbulence intensity also does not have any influence in the inner-torus 2 case. Results of inner-torus 3 behave similarly to the ones of the perfect case. A small deviation is detected at the velocity ratios from 0.50 to 1.00 with the maximal difference at VR=0.57.

For 0.50<VR<1.00, the turbulence intensity has a stronger influence for inner-torus 1 than in the all other cases. Tu% decreases all values of Φ for this case and the highest difference is measured at VR=0.70. For VR>1.00, the influence of the free stream turbulence intensity again becomes almost negligible.

Apparently, the length scales generated by means of the static grid in our experiments are much smaller than the vortical length scales generated by in the jet cross-flow interaction. The free stream turbulence intensity with small length scales does not have any strong influence on the film cooling effectiveness.

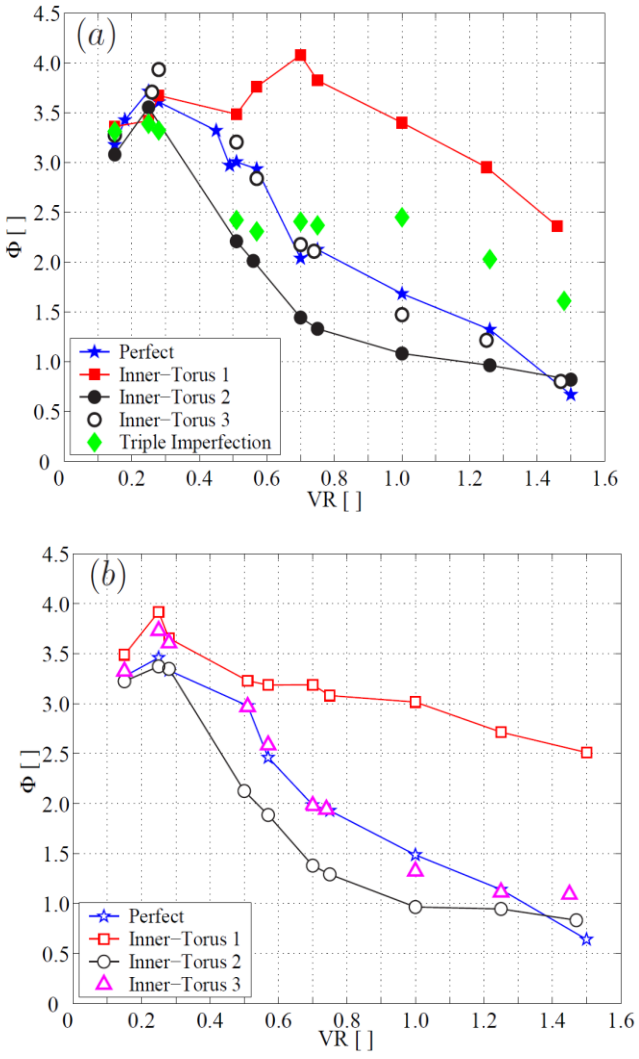

Figure 18: The equivalent cooled surface (Φ) for different inner torus positions at varying velocity ratios (VR) without (top) and with (bottom) turbulence grid.

Sizes and shapes

To investigate how the blockage (blocked surface / surface of the hole) changes the film cooling effectiveness the imperfection blockage is modified. Five imperfections are examined. They make five different blockages of 0.231, 0.352, 0.436, 0.623 and 0.752 for the round imperfections shown in figure 4 (right). Besides, the influence of the use of different imperfection shapes will be investigated. All changed imperfection shapes are tested in the position of inner-torus 2 (so at 1.2D inside the nozzle).

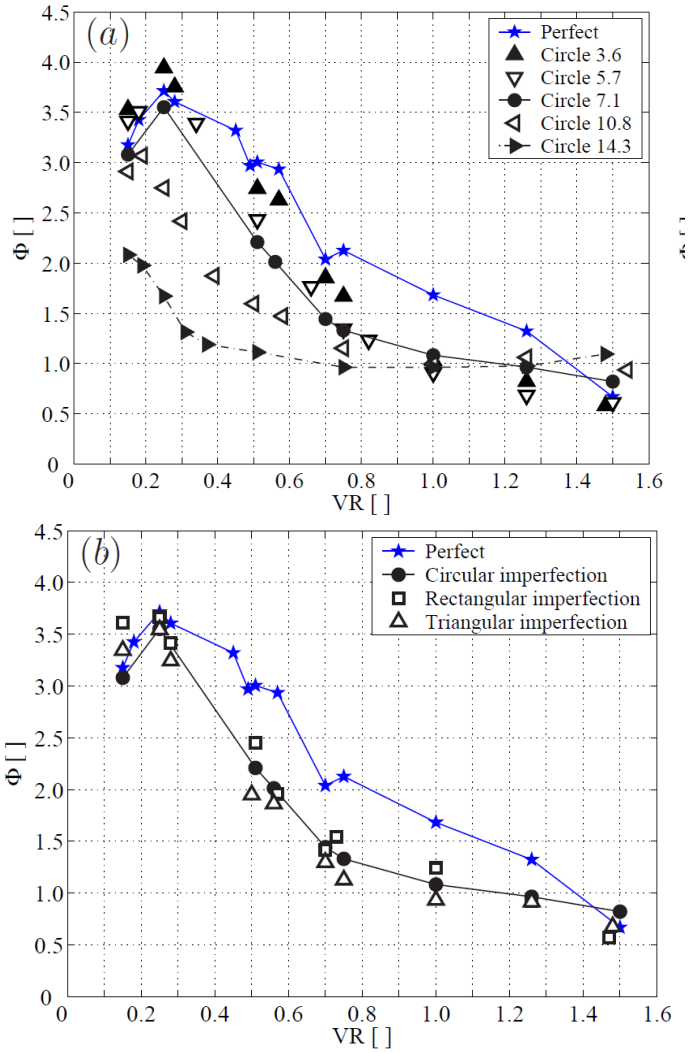

Figure 19: The equivalent cooled surface (Φ) for varying velocity ratios (VR) for changing sizes (top) and shapes (bottom) of the imperfections.

The results for changing blockage are shown in figure 19a. At low velocity ratios, such as VR=0.25, the imperfections which produce smaller blockage do not influence Φ. But the acceleration, which may exceed a factor of 3 for the largest blockage, has a very strong influence and reduces Φ by 55%.

When the velocity ratio is increased, the values of Φ drop in all cases but this drop has different gradients. The gradient is the highest in the perfect case and for the imperfection with the smallest blockage. At the velocity ratio of

0.50, all cases give different values of Φ. The perfect hole generates the highest Φ. Next comes the imperfection with the second smallest blockage. From that point on, Φ decreases with the increase in the blockage at this velocity ratio.

For *VR*=1.00, all equivalent cooled surfaces of the imperfect cases collapse to one point, which lies below the perfect case. For *VR*=1.50, the effect of the imperfection is small but the order is exactly opposite than for *VR*=0.25. The smallest measured Φ is found in the perfect case and in the cases with smaller blockage. The largest Φ is produced using the imperfection with the highest blockage.

To investigate the influence of the cross-sectional shape on the film cooling effectiveness, measurements conducted with the half-torus, rectangular- and triangular imperfections are compared (in figure 19b). The central plane blockage of the imperfection is constant. As may be expected, the influence of the shape is not detected at the small velocity ratios.

For *VR*=0.5, the data starts to scatter. The rectangular imperfection generates the best cooling while the triangular performs the worst. This small scattering reduces with the further increase in the velocity ratio. For *VR*=1.00 exactly the same equivalent cooled surfaces are measured in all three cases. For *VR*=1.50, the data does not collapse to one point but they are within the range of the measurement error. It can be concluded that a cross-sectional shape of the imperfection does not influence the adiabatic film cooling effectiveness.

CONCLUSIONS

The jet, injected through the perfect hole, is studied in detail. Four large vortical structures are detected: the counter rotating vortex pair, windward, lee and spiral vortices. All these structures are quasi-stable. The windward vortices are small and they are a product of a shear layer instability. The lee vortices are generated by the separation over the nozzle trailing edge. Just downstream from the nozzle trailing edge spiral vortices are detected. At velocity ratios larger than 0.75, these vortices mostly mix with the main stream fluid. Therefore, the effectiveness is rather small in the nozzle vicinity when the jet is ejected through the perfect hole. The counter rotating vortex pair is the largest structure, hence most responsible for the momentum and heat transfer. Two vortices, which are generated at the nozzle rimes, warp downstream and form a counter rotating vortex pair due to the jet cross-flow interaction. This structure becomes stronger and larger if the velocity ratio is increased and it is still detected far downstream. Therefore, the velocity ratio has a strong influence on the film cooling effectiveness. At the velocity ratio of 0.50, the jet stays close to the plate wall and it has enough momentum to cover a `long' distance. An increase of the velocity ratio implies a larger and stronger counter rotating vortex pair, which enhances the mixing and the film cooling effectiveness is rapidly reduced.

The influence of the imperfection position on the adiabatic film cooling effectiveness can be neglected at low velocity ratios (smaller than 0.25). The imperfection located 1.2D inside the nozzle (inner-torus 2) decreases effectiveness and narrows the cooled area in comparison with the perfect hole. In this case, the windward vortices are the product of separation over the imperfection and therefore, they originate inside the hole. They are much bigger and stronger than in the perfect case. While larger lee vortices improve the effectiveness in the immediate vicinity of the hole, windward and lee vortices generate a bursting mechanism and the jet collapses in the near field. This collapse directs the fluid of the main stream towards the plate wall and decreases the film cooling effectiveness more than the counter rotating vortex pair in the perfect case. The negative effects of inner-torus 2 vanish at higher velocity ratios (VR > 1.50). At these velocity ratios, the jet penetrates the cross-flow strongly, which enables a large inflow of the main stream into the cooled volume. This inflow strongly decreases the adiabatic effectiveness strongly.

Contrary to inner-torus 2, the imperfection located at the nozzle exit (inner-torus 1) has a positive effect on the cooling effectiveness. It is remarkable that inner-torus 1 enhances the effectiveness 3.5 times at the velocity ratio of 1.50, when compared to the perfect case. The reason is that, although large windward vortices are produced, they do not result into jet bursts. Instead, the jet is pushed more towards the plate wall. Due to the large windward vortices, the counter rotating vortex pair stays closer to the plate wall and becomes unstable. This instability, in combination with the wall vicinity, increases the transport of the jet momentum within the cooled volume and limits the exchange of momentum between the jet and cross-flow fluids. Therefore, the effectiveness is much larger than in the perfect or inner-torus 2 cases.

The adiabatic effectiveness is weakly affected by the turbulent intensity. Only in the case of inner-torus 1, the effectiveness is approximately reduced by 10%. Besides the position, the size, shape and symmetry of imperfections are examined. The film cooling effectiveness for imperfections, placed 1.2D inside the hole, does not depend on the employed cross-sectional shape. The blockage has a very strong influence on the effectiveness at small and moderate velocity ratios (VR<0.75). At higher velocity ratios (VR>1.00) the influence of the size is negligible.

REFERENCES

[1] von Allmen, M. and Blatter, A., Laser-Beam Interaction with Metal, 1995, pp.871-884

[2] Bergeles, G., Gosman, A. D. and Launder, B. E. , The Near-Field Character of a Jet Discharged Normal to a Main Stream, *ASME J. Heat Transfer*, 1976, pp.373-379

[3] Morton, B. R. and Ibbetson, A.,Jets Deflected in a Crossflow, *Thermal and Fluid Science*, 1996, pp.112-133

[4] Fric, T. F. and Roshko, A.,Vortical structure in the wake of a transverse jet, *J. Fluid Mech*., 1994,pp.1-47

[5] Kelso, R. M., Lim, T. T. and Perry, A. E., An experimental study of round jets in cross-flow, *J. Fluid Mech*., 1996, pp.111-114

[6] Lim, T. T., New, T. H. and Luo, S. C., On the development of large-scale structures of a jet normal to a cross flow, *Physics of Fluids*, 2001, pp.770-775